ELSEVIER

Chemical Engineering Science 61 (2006) 3025–3032

Chemical Engineering Science

www.elsevier.com/locate/ces

Numerical simulation of a dissolution process in a stirred tank reactor

H. Hartmann*, J.J. Derksen, H.E.A. van den Akker

Kramers Laboratorium voor Fysische Technologie, Delft University of Technology, Prins Bernhardlaan 6, 2628 BW, Delft, The Netherlands

Received 27 May 2005; received in revised form 30 September 2005; accepted 4 October 2005
Available online 22 December 2005

Abstract

A dissolution process of solid particles suspended in a turbulent flow of a Rushton turbine stirred tank is studied numerically by large eddy simulations including passive scalar transport and particle tracking. The lattice-Boltzmann flow solver and the Smagorinsky subgrid-scale model are adopted for solving the stirred tank flow. To the LES a finite volume scheme is coupled that solves the convection–diffusion equation for the solute. The solid particles are tracked in the Eulerian flow field through solving the dynamic equations of linear and rotational motion of the particles. Particle–particle and particle–wall collisions are included, and the particle transport code is two-way coupled. The simulation has been restricted to a lab-scale tank with a volume equal to 10^{-2} m^3. A set of 7×10^6 spherical particles 0.3 mm in diameter are released in the top part of the tank (10% of the tank volume), resulting in a local initial solids volume fraction of 10%. The particle properties are such that they resemble those of calcium chloride beads. The focus is on solids and scalar concentration distributions, particle size distributions, and the dissolution time. For the particular process considered, the dissolution time is found to be at most one order of magnitude larger than the time needed to fully disperse the solids throughout the tank.

Keywords: Stirred tank; Turbulence; Dissolution; Suspension; Simulation; Particle transport

1. Introduction

Processes in which turbulently agitated solid–liquid suspensions are involved, have a large share in various industrial applications. Examples are crystallization (Hollander et al., 2001), suspension polymerization (initially a liquid–liquid dispersion that in the course of the process turns into a solid–liquid mixture, see e.g. Kiparissides, 1996), particle coating and catalytic slurries. Such processes are very complex multi-phase. In order to improve competitiveness, there is an industrial drive for research on the hydrodynamic phenomena, and their coupling with chemistry and heat and mass transfer. This work aims at a contribution to reliable numerical predictions of complex, multi-phase processes. For this purpose, we focus here on the physical mechanisms occurring in a dissolution process by means of a detailed large eddy simulation (LES) including passive scalar transport and particle tracking.

One of the key aspects in the (dynamic) behavior of the processes mentioned is the role of hydrodynamics. On a macroscopic scale, the hydrodynamic conditions control, e.g. residence time and circulation time in the specific flow system (e.g. a stirred tank). On a microscopic scale, rate-limiting processes such as mass transfer (needed for nucleation and growth in crystallization), agglomeration and attrition (a major source for secondary nucleation), collisions, and the yield of a chemical product (in case of competitive chemical reactions) are largely determined by the smallest-scale flow phenomena.

In this work, the focus is on a dissolution process under strongly turbulent conditions induced by a Rushton turbine in a stirred tank. Because of limited computational resources, the strongly turbulent flow cannot be fully captured by the computational grid. Consequently, direct solving the flow system under consideration goes beyond the present and future foreseeable computational possibilities. As a result, we need to revert to modeling. The basis of the simulation discussed here is a representation of the continuous flow by means of LES. Compared to a Reynolds-averaged Navier–Stokes (RANS) approach, turbulence modeling by means of LES leaves less room for

* Corresponding author. Tel.: +31 15 278 7084; fax: +31 15 278 2838.
E-mail address: h.hartmann@klft.tn.tudelft.nl (H. Hartmann).

0009-2509/$ - see front matter © 2005 Elsevier Ltd. All rights reserved.
doi:10.1016/j.ces.2005.10.058

speculation in modeling the turbulence and the motion of the solids immersed in the flow. Furthermore, the turbulence levels are accurately resolved in an LES compared to a simulation based on the RANS approach. The latter approach underpredicts the turbulence levels by 50% (Hartmann et al., 2004a), which certainly affects the mixing patterns and consequently solid–liquid mixing. Promising LES results of the single-phase flow in a stirred tank have been presented in the past by Eggels (1996), Derksen and Van den Akker (1999), Hartmann et al. (2004b), Hartmann et al. (2004a), Yeoh et al. (2004), and Bakker and Oshinowo (2004).

In the LES flow field, spherical particles are released in the top part of the tank. The motion of the particles and collisions are handled by a solver developed by Derksen (2003). For the inter-phase mass transfer between the disperse and continuous phases, a single-particle correlation of Ranz and Marshall (1952) is applied. Information on the local scalar concentration field, needed for the determination of the mass transfer rate, is obtained by solving the convection–diffusion equation. Exactly as in a LES, the latter equation is solved in an Eulerian framework through a finite volume discretization. The finite volume scheme used in this work has been described by Hartmann (2005).

2. Flow system

The stirred tank used in this work was a standard configuration cylindrical tank of diameter T, with four equi-spaced baffles of width $0.1T$ mounted along the perimeter of the tank. The liquid height was set equal to the tank diameter, $H = T$. The impeller was a six-bladed Rushton turbine with standard dimensions, mounted at height $T/3$. A schematic representation of the flow system is shown in Fig. 1. If geometric similarity is maintained, the single-phase flow can be fully characterized by the Reynolds number ($Re = ND^2/\nu$, with N the impeller speed, D the impeller diameter and ν the viscosity of the continuous phase). In this work, the Reynolds number amounts to 10^5.

The tank volume (V) is set to $10^{-2}\,\mathrm{m}^3$, which implies an impeller diameter of $D = 7.78 \times 10^{-2}\,\mathrm{m}$. The continuous phase is water (with viscosity $\nu = 10^{-6}\,\mathrm{m}^2/\mathrm{s}$ and density $\rho_l = 10^3\,\mathrm{kg/m}^3$). A set of $N_{p0} = 7 \times 10^6$ mono-disperse spherical particles with diameter $d_{p0} = 0.3\,\mathrm{mm}$, and density $\rho_p = 2150\,\mathrm{kg/m}^3$ is released uniformly distributed over the upper part ($0.9T - T$) of the tank. The saturation concentration (c_{sat}) is set to $600\,\mathrm{kg/m}^3$, and the molecular diffusion coefficient (Γ_{mol}) equals $0.7 \times 10^{-9}\,\mathrm{m}^2/\mathrm{s}$, which yields a Schmidt number of about 1400. The settings of the particle diameter, the saturation concentration and the diffusion coefficient are typical for calcium-chloride beads in water. Since calcium ions are larger than chloride ions they have a lower diffusion coefficient. As a result, the diffusion of calcium ions is rate-limiting, and therefore the diffusion coefficient in the simulation is that of calcium ions. The initial solids volume and mass fractions of the set of particles released in the top part of the tank amount to 10% and 21.5%, respectively (the tank average volume and mass fractions are 1% and 2.15%, respectively). The initial macroscopic Stokes number (i.e., the ratio of the Stokesian particle relaxation time and the time of one impeller revolution; $\mathrm{Stk} = (\rho_p/\rho_l)(d_{p0}^2 N/18\nu)$ yields $\mathrm{Stk} = 0.1774$. The initial microscopic Stokes number which relates the Stokesian particle relaxation time to the time scale of the smallest turbulent fluctuations (i.e., the Kolmogorov time scale based on the tank-averaged energy dissipation rate) equals 600. As a result, the particles will initially follow the large-scale turbulent fluctuations. During the course of the simulation, the particle size decreases and the motion of the particle will be influenced by an increasing part of the turbulence spectrum (i.e., the particle will behave more and more as a tracer).

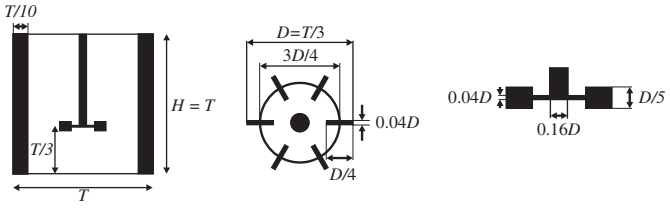

Fig. 1. Cross-section of the tank (left). Plan view and cross-section of the impeller (right). At the top level there is a lid. The impeller is a Rushton turbine mounted at height $T/3$ and has a diameter $T/3$.

The impeller speed is chosen to be above the (initial) just-suspended impeller speed according to the Zwietering (1958) correlation

$$N_{js} = s\,\frac{d_{p0}^{0.2}\,\nu^{0.1}\,(g\Delta\rho)^{0.45}\,\Phi_{m0}^{0.13}}{\rho_l^{0.45}\,D^{0.85}} \tag{1}$$

with g the magnitude of the gravitational acceleration vector, $\Delta\rho = \rho_p - \rho_l$, Φ_{m0} the initial solids mass fraction in %, and s is a constant that equals 8 for the particular configuration. The impeller speed is set to 16.5 rev/s, whereas the (initial) just-suspended speed is 11.4 rev/s. Since the particles dissolve during the course of the simulation, the particle size and solids mass fraction decreases in time, and consequently the just-suspended speed decreases.

3. Simulation procedure

We apply LES, as the strongly turbulent flow ($Re = 10^5$) cannot be fully recovered by the computational grid. The Smagorinsky (1963) model has been used to include the effect of the subgrid-scale velocity fluctuations on the larger flow scales. For more details on the LES methodology embedded within the lattice-Boltzmann discretization scheme we refer to Hartmann et al. (2004a), Derksen and Van den Akker (1999), Chen and Doolen (1998) and Somers (1993).

The particle transport solver used for the simulation of the dissolution process makes use of the Eulerian–Lagrangian approach and has been developed by Derksen (2003). For the determination of the drag force, subgrid-scale velocity fluctuations have been included by means of a Gaussian random process. Next to the solution of the solid particles dynamics, particle–wall, particle–impeller and particle–particle collisions are considered in the solver. The latter mechanism proved to

be crucial in order to obtain a realistic particle distribution throughout the tank (Derksen, 2003).

Mass transfer is controlled by a mass transfer coefficient (k) and a driving force, which is the difference between the saturation concentration (c_{sat}) and the concentration of the surroundings (c)

$$\dot{m}_{\mathrm{int}} = kA(c_{\mathrm{sat}} - c), \tag{2}$$

where $\dot{m}_{\mathrm{int}}$ is the inter-phase mass transfer rate between the particle and liquid, and $A = \pi d_p^2$ is the surface of the spherical particle. The mass transfer coefficient can be written as

$$k = Sh\,\frac{\Gamma_{\mathrm{mol}}}{d_p}, \tag{3}$$

where Sh is the Sherwood number. In this work, Ranz and Marshall (1952) correlation is used for the calculation of the Sherwood number

$$Sh = 2.0 + 0.6 Re_p^{1/2} Sc^{1/3}, \tag{4}$$

where Re_p is the particle Reynolds number, defined as

$$Re_p = \frac{v_{\mathrm{sl}} d_p}{\nu}, \tag{5}$$

where v_{sl} is the slip velocity (i.e., the magnitude of the velocity of the particle relative to the fluid).

The concentration of the surroundings in Eq. (2) is assumed to be the average concentration in the control volume. The effect of concentration fluctuations at the subgrid-scale level on the mass transfer rate has been ignored, since the mass transfer rate linearly scales with the concentration (see Eq. (2)), and the effect of fluctuations tends to average out. The cell-averaged concentration is determined via the discrete solution of the convection–diffusion equation. This is achieved by coupling a scalar mixing solver to the LES and particle transport solvers.

Eggels and Somers (1995) have performed scalar transport calculations on free convection cavity flow with the lattice-Boltzmann discretization scheme. This scheme, however, is more memory intensive than a finite volume formulation of the convection–diffusion equation. Therefore, we have coupled a compressible finite volume discretization scheme for the scalar transport to the compressible lattice-Boltzmann scheme. The convection–diffusion equation in compressible form reads

$$\frac{\partial \rho_l c}{\partial t} + \frac{\partial u_i \rho_l c}{\partial x_i} = \frac{\partial}{\partial x_i}\left(\rho_l \Gamma \frac{\partial c}{\partial x_i}\right) + S_c, \tag{6}$$

where ρ_l is the density of the continuous phase, c is the scalar concentration, u_i is velocity component i, Γ is the diffusion coefficient and S_c is a source term. Note the summation over the repeated index i. The diffusion coefficient is the sum of the molecular and eddy diffusion coefficients: $\Gamma = \Gamma_{\mathrm{mol}} + \Gamma_e$. The eddy diffusion coefficient is related to the eddy viscosity via a turbulent Schmidt number (Sc_t) through $\Gamma_e = \nu_e / Sc_t$. For the turbulent Schmidt number we have chosen a value of 0.7. The finite volume solver used in the context of this work has been described in detail by Hartmann (2005). It contains a high-resolution flux-limited TVD scheme (Total Variation Diminishing, see Harten, 1983) for minimizing numerical diffusion.

The discretized source term $S_{c,i}$ describes inter-phase mass transfer and reads

$$S_{c,i} = \rho_l \Delta V^{-1} \sum_{j=1}^{N_{p,i}} \dot{m}_{\mathrm{int},j}, \tag{7}$$

where ΔV is the volume of cell i (which is the same for all cells in the uniform, cubic grid), $N_{p,i}$ is the number of particles with their center of mass in cell i and $\dot{m}_{\mathrm{int},j}$ is the inter-phase mass transfer rate (see Eq. (2)) between particle j and the surrounding continuous phase. The diameter of particle j is adjusted each time step as follows:

$$d_{p,j}^{n+1} = \sqrt[3]{(d_{p,j}^{n})^3 - \frac{6}{\pi}\rho_p^{-1}\dot{m}_{\mathrm{int},j}\Delta t}, \tag{8}$$

where Δt is the time step.

The code runs on the parallel computer platform 'Aster' located at SARA in Amsterdam. Aster is an SGI Altrix 3700 system, consisting of 416 CPUs (Intel Itanium 2, 1.3 GHz, 3 Mbyte cache each), 832 Gbyte of memory and 2.8 Tbyte of scratch disk space. The total peak performance is 2.2 Teraflop/s. Within the parallel environment of 'Aster' the code makes use of domain decomposition: the computational domain was horizontally split in 30 equally-sized subdomains (i.e., normal to the tank centerline). Dynamic load-balancing was not implemented in the code. This initially results in a poor parallel efficiency and a low calculation speed, as all particles are located in the upper subdomains. Gradually, the calculation speed increases due to dispersion of the particles throughout the tank, and due to the dissolution process causing a decreasing load of the collision algorithm. The MPI message passing tool has been used for communication between the subdomains.

The particles are released in a quasi steady-state flow field. The scalar concentration at the start of the simulation equals zero throughout the tank. The simulation has been executed on a cubic, Cartesian grid of 240^3 lattice cells. The diameter of the tank equals 240 lattice spacings, resulting in a spatial resolution of 0.973 mm. The temporal resolution is limited by the lattice-Boltzmann method. The tip speed of the impeller is set to 0.1 lattice spacings per time step in order to meet the incompressibility limit. This results in a temporal resolution of 25 μs. Inside the computational domain, the no-slip boundary conditions for the velocity components at the cylindrical tank wall, the baffles, the impeller, and the impeller shaft were imposed by an adaptive force-field technique (Derksen and Van den Akker, 1999). The zero-gradient boundary condition for the scalar concentration at the (moving) walls has been imposed via a newly developed immersed boundary technique (Hartmann, 2005). The total memory requirements of the simulation resulted in an executable of about 2.5 GByte. The full simulation of 100 impeller revolutions took about 6 weeks.

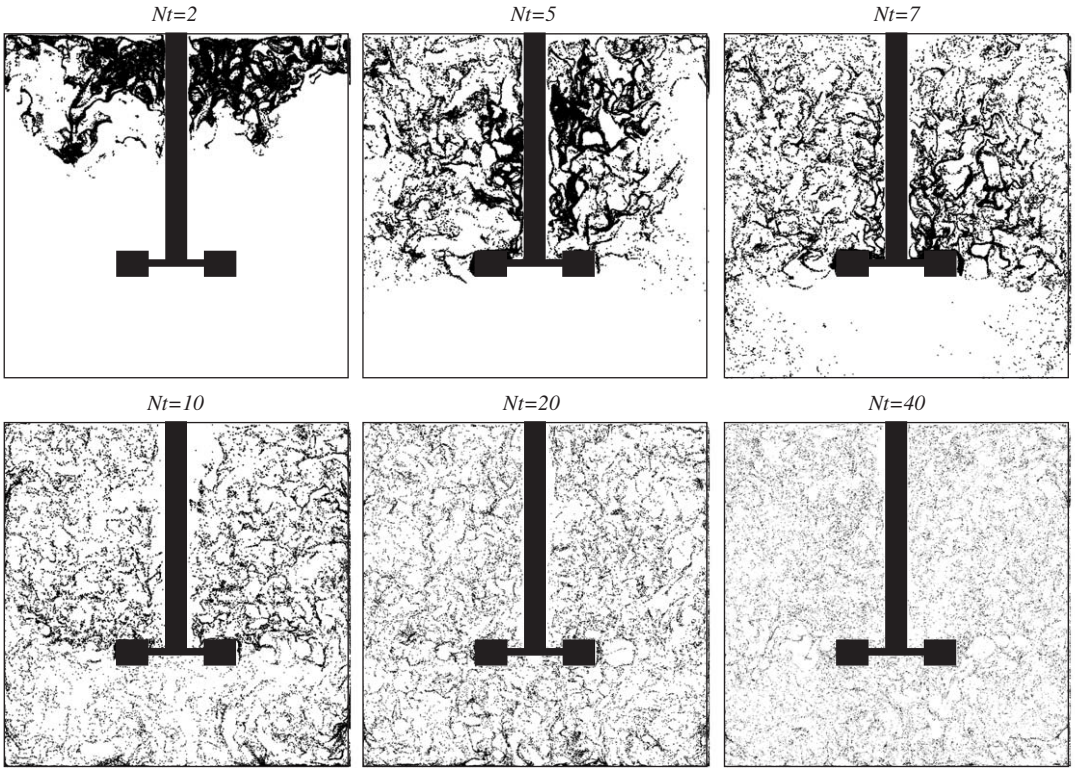

Fig. 2. Snapshots of the particle distribution in a vertical plane mid-way between two baffles. In the graphs, the particles in a slice with thickness $T/240$ have been displayed. The diameter of the particles is 3 times enlarged for clarity. The respective concentration distributions are shown in Fig. 3.

4. Results

4.1. Snapshots of the particle distributions and concentration fields

Figs. 2 and 3 give an impression of the dissolution process during the course of the simulation. The scalar concentrations are normalized with the final concentration c_∞ defined as

$$c_\infty = \frac{M_{p0}}{V} = \frac{2}{3} N_{p0} \rho_p \left(\frac{d_{p0}}{T} \right)^3, \tag{9}$$

where $M_{p0} = N_{p0} \rho_p (\pi/6) d_{p0}^3$ is the total particle mass at $Nt = 0$.

During the first 5 impeller revolutions, the particles are transported toward the impeller region. High particle concentrations are accompanied by high scalar concentrations, and a clear interaction between the particles and turbulence is identified. The particles are swept radially outward by the revolving impeller, and are subsequently entrained in the lower recirculation loop. In the next 5 impeller revolutions, the particles are distributed throughout the tank. During the first 10 impeller revolutions, clear macroscopic scalar concentration structures are identified.

The snapshots of the particle distributions at $Nt = 10$ and 20 show high particle concentrations at the bottom and outer walls. Because of the particle inertia and the density of the particles being higher than that of the liquid, the particles are swept out of the high-vorticity regions (streaky patterns). Due to a decreasing solid particle mass during the process, the particle inertia decreases (the streaky patterns die out), the particles residing at the bottom are more easily resuspended (compare the snapshots at $Nt = 20$ and 40), and the particle distribution is becoming more and more homogeneous.

For $Nt > 10$, the macroscopic structures in the scalar concentration have disappeared (see Fig. 3). A decrease of the particle mass observed in the snapshots in Fig. 2 is associated with an increase of scalar concentration. At the wall separation points and at the bottom of the tank spots of high concentration are observed that correspond with local high solids concentrations.

In Fig. 4 two snapshots of the particle distribution at $Nt = 26.5$ and 60 are shown. The particle distribution at $Nt = 26.5$ shows an axial gradient in the average particle size. The particles transported in the lower recirculation zones are generally smaller than the particles transported in the upper recirculation zone. The reason for this effect is that compared with the upper recirculation loop, the lower recirculation loop is stronger and this induces an increased mass transfer rate. A comparison between the upper and lower graphs clearly shows the difference in particle size. The spatial particle distribution at $Nt = 60$ is nearly homogeneous.

The snapshot of the particle distribution at $Nt = 26.5$ shows a region void of particles extending from the bottom to closely underneath the impeller, slightly right from the tank centerline. This region is associated with a slowly precessing vortex that crosses the cross-section. This precessing vortex, here in

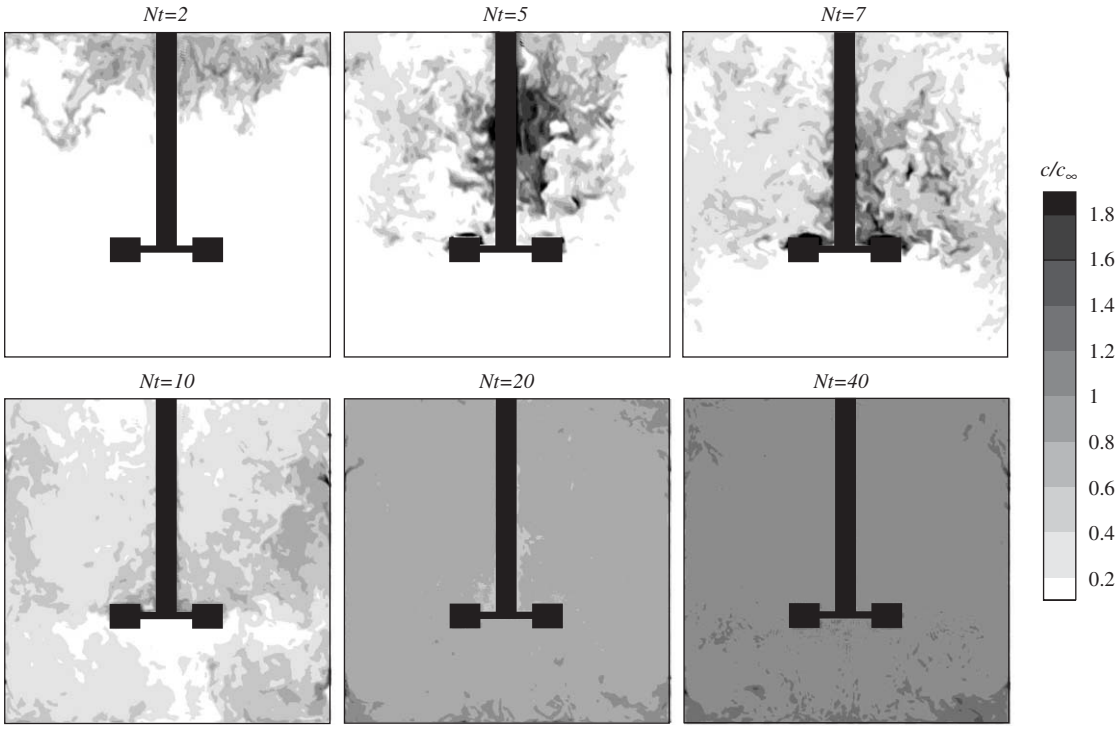

Fig. 3. Snapshots of the concentration distribution in a vertical plane mid-way between two baffles. The respective particle distributions are shown in Fig. 2.

interaction with the particles, is the manifestation of a macro-instability (see Hartmann et al., 2004b; Nikiforaki et al., 2002).

4.2. Stages in the dissolution process

Fig. 5 shows time-traces of the number of particles in ten axial slices of height $0.1T$, with a focus on the top and bottom slices. Based on the observations in the previous subsection and the path of the curves shown in Fig. 5, five stages can be identified: (Stage I; $0 \leqslant Nt < 12$) Mixing and dispersing, (Stage II; $12 \leqslant Nt < 24$) Quasi steady-state, (Stage III; $24 \leqslant Nt < 42$) Resuspension, (Stage IV; $Nt \geqslant 42$) Dissolution, and (Stage V; $Nt \geqslant 58$) Homogeneous suspension.

In stage I (mixing and dispersing), the solids are distributed throughout the tank till a quasi steady-state situation is reached (stage II). During stage II, the dissolution process proceeds, but the number of particles in all slices remains approximately constant. The number of particles in the bottom slice is about 1.6–2.3 times higher than the number of particles in the other slices. At $Nt = 24$ the number of particles in the bottom slice starts to decrease significantly (stage III), as the particles get more easily resuspended due to their decreased size. After about 42 impeller revolutions, the first particle is fully dissolved (the onset of stage IV). Stage V is a part of stage IV and starts at the time instant $Nt = 58$ when a fully homogeneous suspension is reached. For the particular case studied here, the time to dissolve all particles (i.e., the dissolution time) is at most one order of magnitude larger than the time to distribute the particles throughout the tank.

4.3. Evolution of particle size distribution in time

In Fig. 6 the particle size distributions are shown at nine instants in time. The first six distributions correspond to the particle distributions shown in Fig. 2. During the course of the simulation, the particle size distribution broadens and shifts toward smaller particle sizes. At $Nt = 60$, 80, 100 a peak is observed in the first bin, representing the number of dissolved particles (i.e., 16.8%, 97.3%, 99.9% of the total amount of particles released).

A peculiar feature of the particle size distributions at $Nt = 60$, 80 and 100 is its steep slope at the smallest particle sizes. This can be explained by Eqs. (2) and (3). As $d_p \to 0$ the Sherwood number approaches 2. Consequently, the mass flux scales as d_p^{-1}, and the mass transfer rate as d_p. A mass conservation equation describing the inter-phase mass transport results in the time derivative of the particle diameter to scale with d_p^{-1}. As a result, the particle size distribution collapses faster at low particle sizes than at higher particle sizes. This effect relates to the slight increase of the Sauter diameter ($d_{32} = (\sum_{i=1}^{N_p} d_{p,i}^3)/(\sum_{i=1}^{N_p} d_{p,i}^2)$) seen in the final stage of the dissolution process (see Fig. 7).

4.4. Dissolution time

The dissolution time is the time needed to fully dissolve all the solids. In a numerical simulation including particle tracking, the total number of solid particles is monitored, and hence the dissolution time is the time when the total number of particles has reached the zero value.

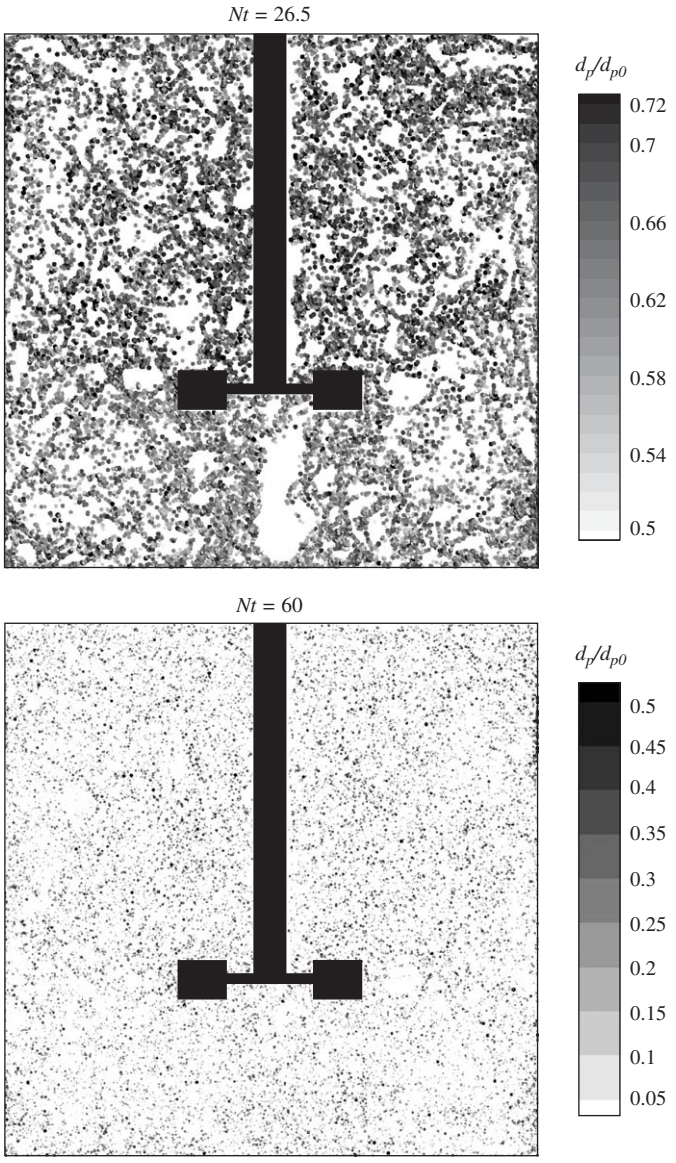

Fig. 4. Snapshots of the particle distribution in a vertical mid-way baffle plane. In the graphs, the particles in a slice with thickness $T/240$ have been displayed. The diameter of the particles is 10 times enlarged for clarity, and the colors represent the dimensionless particle diameter.

In Fig. 8 the evolution of the total number of particles normalized with the number of released particles as a function of time is shown. The dissolution process starts at Nt=42.5 (not shown), and from $Nt = 50$ a steep decrease in the number of particles is observed till $Nt = 70$. The simulation was stopped at $Nt = 100$ when less than 0.1% of the total amount of released particles was left. With a view to a sensible use of computational effort, it is not believed that any valuable information apart from the dissolution time is to be found for $Nt > 100$. The time instant where 99% of the particles is dissolved is $\theta_{s,99\%} = 84N^{-1}$.

4.5. Time series of concentration

In Fig. 9, time series of the scalar concentration are shown, recorded at two monitoring points. One monitoring point is

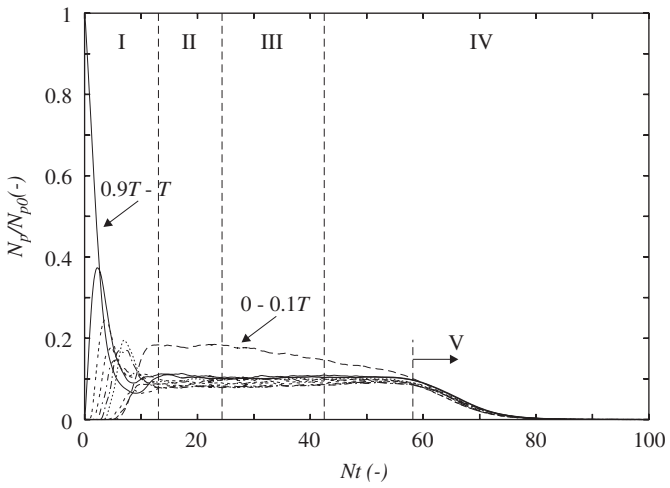

Fig. 5. Evolution of particle number in ten axial slices of height $0.1T$. The focus is on the top and bottom slices. Five stages in the dissolution process can be defined: Mixing and dispersing (I), Quasi-steady-state (II), Resuspension (III), and Dissolution (IV). At time instant Nt=58 a more-or-less homogeneous suspension is reached (Stage V).

located in the upper recirculation loop (i.e., in a mid-way baffle plane at $z/T = 0.67$ and $r/T = 0.25$), and the other in the lower recirculation loop (i.e., in a mid-way baffle plane at $z/T = 0.19$ and $r/T = 0.25$). In the first 12–15 impeller revolutions strong concentration fluctuations are observed, which correspond with the macroscopic structures seen in Fig. 3. The concentration fluctuations registered at the monitoring point at $z/T = 0.67$ (solid line Fig. 9) are stronger compared to those at the monitoring point at $z/T = 0.19$ (dashed line in Fig. 9). This is because the particles were released in the top part of the tank.

Subsequently for $Nt > 15$, the concentration recorded at both monitoring points gradually increases to a final level of about $1.12c_\infty$. The significant, unphysical scalar mass increase of 12% in 100 impeller revolutions is due to our (novel) immersed boundary technique for the scalar concentration to impose a zero-gradient constraint at the walls that are off-grid (see Hartmann, 2005). At the current grid resolution, the technique is unable to accurately represent the edges of the impeller blades, impeller disk and baffles. In future research, the immersed boundary technique needs to be improved. Possible solutions for better conserving scalar mass are (local) grid refinement, and the use of a cylindrical grid by the scalar transport solver.

5. Conclusions

A simulation of a dissolution process (i.e., a solid–liquid suspension) according to an Eulerian–Lagrangian approach has been presented in this paper. Under the action of a driving force (i.e., the difference between the saturation concentration and the concentration of the surroundings) and a mass transfer coefficient (depending on the particle slip velocity) the 7 million solid, spherical particles, slowly dissolved during the course of the simulation. The effect of subgrid-scale concentration fluctuations on the mass transfer rate has been ignored.

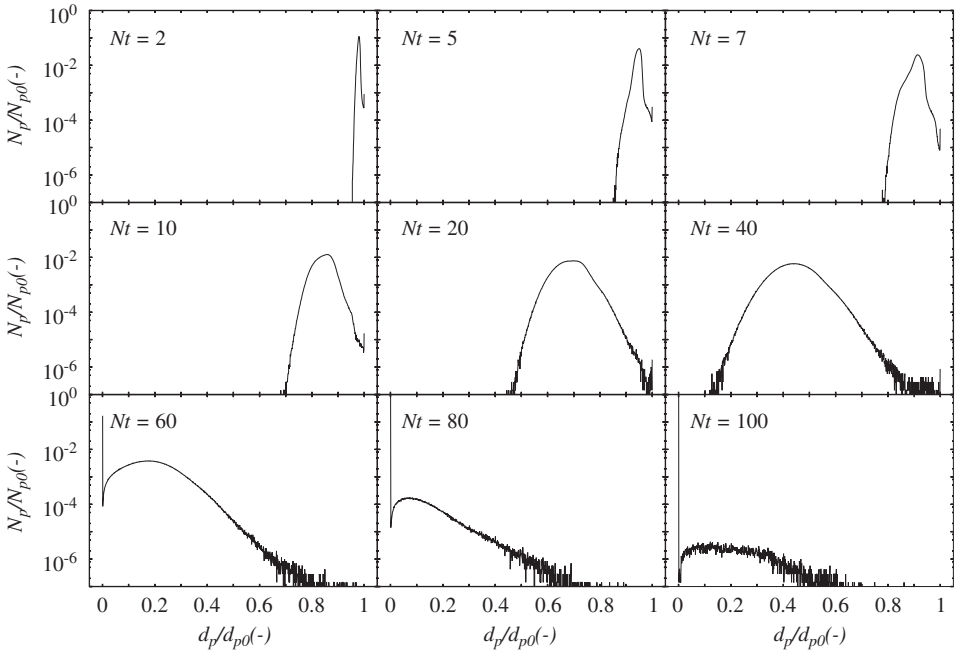

Fig. 6. Instantaneous realizations of the particle size distribution (lin-log plots).

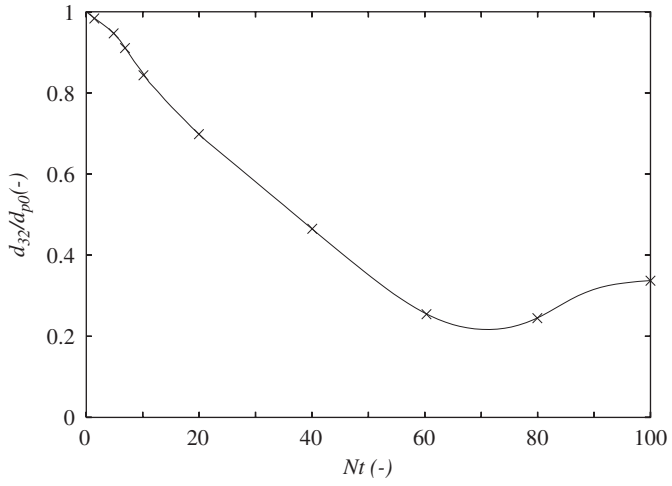

Fig. 7. Evolution of the Sauter mean diameter in time. The crosses correspond with the particle size distributions shown in Fig. 5.

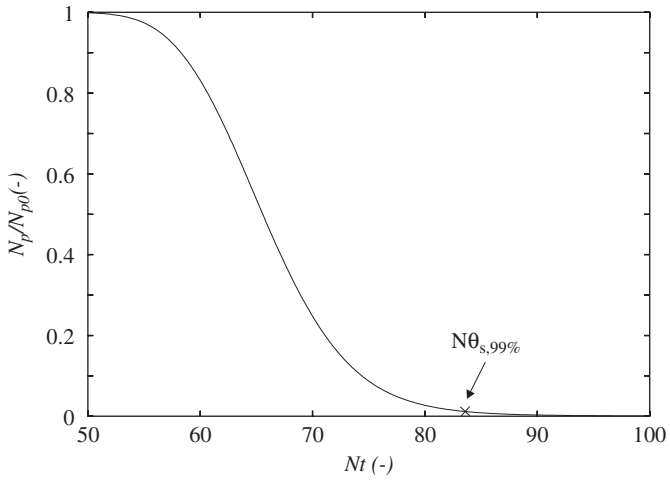

Fig. 8. Evolution of number of particles throughout the tank in time, starting at $Nt = 50$.

Various stages in the dissolution process considered in this work have been identified by means of snapshots of the solids and scalar concentration distributions, and time series of the particle number in ten axial slices of width $0.1T$. In the first stage (0–12 impeller revolutions), the particles are dispersed throughout the tank. Subsequently, the system is in a quasi steady-state situation (i.e., the second stage, 12–24 impeller revolutions). In these two stages, the particles organize in streaky patterns, by leaving high-vorticity regions. Furthermore, high solids and scalar concentrations are found below the impeller, at the bottom of the tank, in front of the impeller blades, at the outer walls, and at the wall separation points. Large regions void of particles are observed behind the impeller blades.

The decrease of the particle mass in the course of the process has two important implications. In the first place, the high particle concentration at the bottom of the tank disappears as the particles get resuspended. Secondly, the streaky patterns disappear due to decreasing inertia of the particles. These observations occur in the third stage (i.e., 24–42 impeller revolutions). The fourth and final stage covers the dissolution of the particles. At roughly 58 impeller revolutions a homogeneous solids suspension is reached.

The non-homogeneous mixing and consequently mass transfer in a stirred tank reactor is expressed in the evolution of the particle size distribution. During the course of the simulation, the particle size distribution broadens and moves to lower

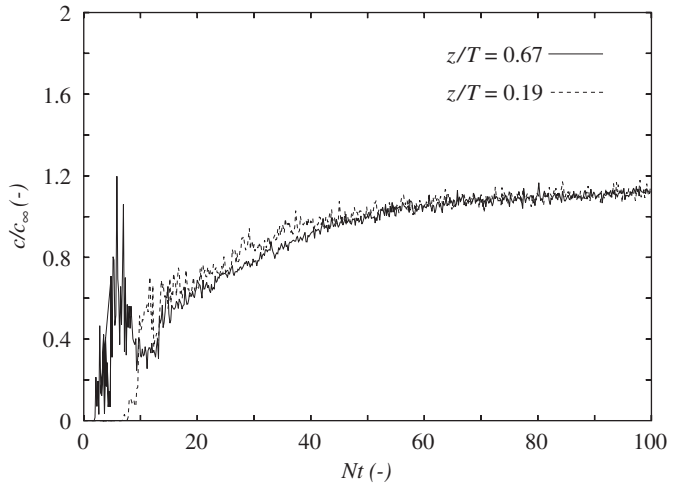

Fig. 9. Simulated time traces of the concentration normalized with the final concentration c_∞. The two monitoring points are at a radial position $r/T = 0.25$ in a mid-way baffle plane.

particle diameters. The peculiar steep slope observed at the smallest particle sizes is due to the mass transfer rate increasing at decreasing particle diameter for very small particles. This latter effect causes the slight increase of the Sauter diameter in the final stage of the process.

Time traces of the concentration show in the first 15 impeller revolutions strong concentration fluctuations, and subsequently a slow increase of the concentration toward $1.12c_\infty$. The artificially higher concentration provides a reduced mass transfer rate, and consequently an overprediction of the dissolution time. In the present case studied, the final concentration is a factor 30 lower than the saturation concentration. As a result, the overprediction of the dissolution time is expected to be marginal (only 0.5% based on a back-of-the-envelope calculation). The significant, unphysical increase of scalar mass of 12% is attributed to our (novel) immersed boundary technique. At the current grid resolution, the impeller blade, the impeller disk, and the baffle edges are not accurately recovered.

There are still quite some issues open for improvement with respect to the modeling attempt here. The volume fraction occupied by the particles, which is significant in the first stages of the dispersion, has not been taken into account. For further issues related to the particle transport solver we refer to the paper of Derksen (2003). The mass leakage into the system induced by our (novel) immersed boundary technique may be repaired by (local) grid refinement or the usage of a cylindrical grid in case of the scalar transport solver.

The simulation of a dissolution process through LES including passive scalar transport and particle tracking gave a detailed insight in the complex phenomena (i.e., the intricate interplay of turbulence, mass transfer, motion of particles, collisions, etc.) occurring during the process. For the process considered in this work, it has been shown that the dissolution time is at most one order of magnitude longer than the dispersion time scale. The current successful application of the coupled LES/particle transport/scalar mixing solvers opens worthwhile future directions of numerical research like crystallization processes.

Acknowledgements

This work was sponsored by the Netherlands National Computing Facilities for the use of supercomputer facilities, with financial support from the Netherlands Organization for Scientific Research (NWO).

References

Bakker, A., Oshinowo, L.M., 2004. Modelling of turbulence in stirred vessels using large eddy simulation. Chemical Engineering Research and Design A9, 1169–1178.

Chen, S., Doolen, G.D., 1998. Lattice–Boltzmann method for fluid flows. Annual Review of Fluid Mechanics 30, 329–364.

Derksen, J.J., 2003. Numerical simulation of solids suspension in a stirred tank. A.I.Ch.E. Journal 49 (11), 2700–2714.

Derksen, J.J., Van den Akker, H.E.A., 1999. Large eddy simulations on the flow driven by a Rushton turbine. A.I.Ch.E. Journal 45 (2), 209–221.

Eggels, J.G.M., 1996. Direct and large eddy simulations of turbulent fluid flow using the lattice-Boltzmann scheme. International Journal of Heat and Fluid Flow 17, 307–323.

Eggels, J.G.M., Somers, J.A., 1995. Numerical simulation of free convective flow using the lattice-Boltzmann scheme. International Journal of Heat and Fluid Flow 16 (5), 357–364.

Harten, A., 1983. High resolution schemes for hyperbolic conservation laws. Journal of Computational Physics 49, 357–393.

Hartmann, H., 2005. Detailed simulations of liquid and solid-liquid mixing. Turbulent agitated flow and mass transfer. Ph.D. thesis (ISBN 90-6464-234-6), Delft University of Technology, The Netherlands.

Hartmann, H., Derksen, J.J., Montavon, C., Pearson, J., Hamill, I.S., Van den Akker, H.E.A., 2004a. Assessment of large eddy and RANS stirred tank simulations by means of LDA. Chemical Engineering Science 59 (12), 2419–2432.

Hartmann, H., Derksen, J.J., Van den Akker, H.E.A., 2004b. Macro-instability uncovered in a Rushton turbine stirred tank. A.I.Ch.E. Journal 50 (10), 2383–2393.

Hollander, E.D., Derksen, J.J., Portela, L.M., Van den Akker, H.E.A., 2001. Numerical scale-up study for orthokinetic agglomeration in stirred vessels. A.I.Ch.E. Journal 47, 2425–2440.

Kiparissides, C., 1996. Polymerization modelling: a review of recent developments and future directions. Chemical Engineering Science 51, 1637.

Nikiforaki, L., Montante, G., Lee, K.C., Yianneskis, M., 2002. On the origin, frequency and magnitude of macro-instabilities of the flows in stirred vessels. Chemical Engineering Science 58 (13), 2937–2949.

Ranz, W.E., Marshall, W.R., 1952. Evaporation from drops. Chemical Engineering Progress 48, 142–180.

Smagorinsky, J., 1963. General circulation experiments with the primitive equations: 1. The basic experiment. Monthly Weather Review 91, 99–164.

Somers, J.A., 1993. Direct simulations of fluid flow with cellular automata and the lattice-Boltzmann equation. Applied Scientific Research 51, 127–133.

Yeoh, S.L., Papadakis, G., Lee, K.C., Yianneskis, M., 2004. Large eddy simulation of turbulent flow in a rushton impeller stirred reactor with sliding-deforming mesh methodology. Chemical Engineering and Technology 27 (3), 257–263.

Zwietering, T.N., 1958. Suspending of solid particles in liquid by agitators. Chemical Engineering Science 8, 244.